Journal of Materials Chemistry A

Accepted Manuscript

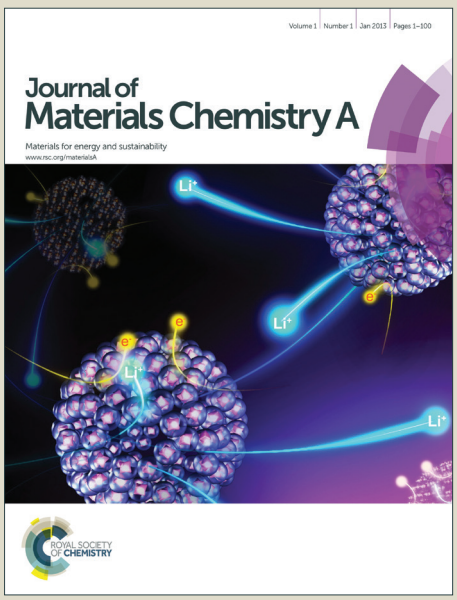

ROYAL SOCIETY OF CHEMISTRY

www.rsc.org/materialsA

Journal of Materials Chemistry A

Remarkable chemical adsorption of manganese-doped titanate for direct carbon dioxide electrolysis

Wentao Qi [a#], Yun Gan [#a], Di Yin [#b], Zhenyu Li [b], Guojian Wu [a], Kui Xie*[a], Yucheng Wu*[a]

Received (in XXX, XXX) Xth XXXXXXXXX 20XX, Accepted Xth XXXXXXXXX 20XX
DOI: 10.1039/b000000x

Chemical adsorption of CO_2 in composite cathode at high temperature plays a significant role for the electrochemical conversion of CO_2 into fuels in the efficient solid oxide electrolysers. In this work, the active Mn with multi oxidation states is introduced into the B-site lattice of the redox-stable $(La,Sr)TiO_{3+\delta}$ to create oxygen vacancies both in the bulk and on the surface. The ionic conductivities of the Mn-doped titanate are remarkably enhanced by 1-2 orders of magnitude at intermediate temperatures in reducing or oxidizing atmospheres. The chemical adsorption of CO_2 is accordingly enhanced by approximately 1 order of magnitude for the Mn-doped titanate and the onset temperature of strong chemical desorption is consequently extended to as high as approximately 800 °C of the common operation temperature of solid oxide carbon dioxide electrolysers. First principles calculations reveal that the oxygen vacancy defect sites created by Mn dopant substantially contribute to the chemical adsorption of CO_2 and the strong bonding of the oxide ions in CO_2 to the nearest cations on the $(La,Sr)O$- or $(Ti,Mn)O_2$-terminated facets not only activates CO_2 molecules but also considerably increases the desorption temperature. The highest current efficiencies of approximately 100% are obtained with the Mn-doped titanate cathode for the direct electrolysis of CO_2 in an oxide-ion-conducting solid oxide electrolyser.

Introduction

Solid oxide electrolysers have demonstrated the tremendous advantages of electrochemical conversion of CO_2 into fuels with high efficiencies using renewable electrical energy [1-2]. The oxide-ion-conducting solid oxide electrolysers can directly electrolyze carbon dioxide into carbon monoxide and pure oxygen under external applied potentials. At the cathode, the CO_2 molecules are electrochemically reduced and split into CO while the generated O^{2-} ions are transported through the electrolyte membrane to the anode compartment where the pure O_2 gas is formed and released.

Conventional Ni-YSZ has been preferentially used as composite cathode in the oxide-ion-conducting solid oxide electrolysers for high-temperature electrolysis [3-6]. However, the inherent redox instability of Ni-YSZ remains an unsolved problem and a significant concentration of reducing gas has to be fed at the cathode to prevent the oxidation of Ni into NiO when operating high-temperature electrolysis. Otherwise, the oxidation of the Ni in this process leads to the loss of the electrical conductivity, degradation of the electrode performance and even delaminations of the electrode layer from the electrolyte surfaces [7-8]. In contrast to Ni-YSZ, the perovskite-type $La_xSr_{1-x}Cr_yMn_{1-y}O_{3-\delta}$ (LSCM) is an active and redox stable material which has been utilized for the direct high-temperature electrolysis and promising electrode polarizations have been achieved [9-10]. We have recently demonstrated the direct high-temperature electrolysis of CO_2 using LSCM cathode without the flow of reducing gas over the electrode in an oxide-ion-conducting solid oxide electrolysers and found that the strong reducing potentials required for CO_2 splitting cause the chemical and structural changes of the p-type LSCM and therefore exhibit large electrode polarization resistance and decreased Faradic current efficiencies at high applied potentials [11-12].

The perovskite titanate, e.g., $La_xSr_{1-x}TiO_{3+\delta}$ (LSTO), is an active, redox-stable material with high n-type conductivity upon reduction, which has been proved to be an alternative electrode material for solid oxide electrolyser [13]. In addition, the A-site deficiency in $La_xSr_{1-x}TiO_{3+\delta}$, e.g., $La_{0.4}Sr_{0.4}TiO_3$, results in an increased electronic conductivity of $La_xSr_{1-x}TiO_{3+\delta}$ under reducing conditions [14]. Composite cathode based on $La_{0.2}Sr_{0.8}TiO_{3.1}$ has been confirmed to be well adapted to the reducing condition for the efficient electrolysis of CO_2 in an oxygen-ion conducting solid oxide electrolyser because the $La_xSr_{1-x}TiO_{3+\delta}$ is partially electrochemically reduced ($Ti^{4+}\rightarrow Ti^{3+}$) at potentials required for CO_2 reduction and the n-type electronic conduction of composite cathode is accordingly enhanced [15]. The active Ti^{3+} is a catalytic-active site which is expected to further improve the cathode performances with favorable kinetics. The perovskite $La_xSr_{1-x}TiO_{3+\delta}$ has a superior resistance to carbon formation and sulfur poisoning, thus is versatile in electrolysis mode running for direct electrolysis of carbon dioxide.

In a solid oxide carbon dioxide electrolyser, the insufficient adsorption of CO_2 is always the limitation at high temperature that leads to the local starvation of CO_2 and therefore restricts the cell performance and current efficiency because the linear CO_2 molecules without any polarity are hard to be chemically adsorbed and activated especially at high temperatures [16-17]. It is common to observe that the local starvation of CO_2 mainly leads to the large electrode polarizations and low current efficiencies for the electrolysis of CO_2 at high temperature. It is reported that the mass transfer is always the limiting step of the electrolysis of CO_2 at higher applied potentials according to their *in-situ* ac impedance studies and the nano-structured composite cathode with extended three-phase boundaries can relieve the local starvation of CO_2 to some extent [18-19]. In order to improve the conversion of CO_2, steam electrolysis is also simultaneously and tentatively conducted with the electrolysis of CO_2 to make use of the *in-situ* water gas shift reaction to enhance the conversion of CO_2 to CO and generate a mixture of CO and H_2 [20]. It is found that the produced H_2 from steam electrolysis reduces the CO_2 into CO accompanied by the formation of H_2O according to the thermal equilibriums of the reversible water gas

shift reactions. However, the direct electrolysis of CO_2 is still a big challenge because the bottleneck of the chemical adsorption of CO_2 on the surface of the ceramic cathode skeletons substantially restricts the species adsorption, desorption and transfer in the composite cathode and hence decrease the direct electrolysis performances and efficiencies.

Currently preferred chemical adsorption of CO_2 on solid materials are based on grafting solid amine and producing alkaline surface; however, the desorption temperature are normally below 300 °C which is far below the operation temperature of solid oxide electrolysers [21-23]. It is also reported that some basic sites can be produced on the surface of solid oxide materials, e.g., TiO_2, after strong reduction for the adsorption of CO_2 [24-25]. Though the onset temperature of chemical desorption of CO_2 can be extended to as high as 400-500°C this is still not high enough for the composite cathodes of solid oxide electrolyzers. Defected sites with oxygen vacancies on the surface of solid oxide materials provide the promising possibilities for the chemical adsorption of CO_2 as these sites could act as host sites to accommodate the linear CO_2 molecules [26], which is expected to significantly extend the onset temperature of chemical desorption of CO_2 and benefit the solid oxide electrolyzer cathode. On the other hand, the chemically adsorbed CO_2 molecules are expected to be strongly activated on these vacancy-related defect sites and favorable for their electrochemical reduction at high temperatures.

In this work, the redox-active Mn with multi oxidation states is introduced into the B-site of the redox-stable $(La,Sr)TiO_{3+\delta}$ perovskite to create the oxygen vacancies both in the bulk and on the surface for the chemical adsorption of CO_2 molecules. The electrical properties and the chemical adsorption/desorption of CO_2 of the Mn-doped $(La,Sr)TiO_{3+\delta}$ are systematically studied. Direct electrolysis of CO_2 with the cathode based on the Mn-doped $(La,Sr)TiO_{3+\delta}$ is performed and studied in an oxide-ion conducting solid oxide electrolyser.

Experimental

All the chemicals were bought from SINOPHARM Chemical Reagent Co.Ltd (China) except specifically specified. The $La_{0.2}Sr_{0.8}TiO_{3+\delta}$ (LSTO) and $La_{0.2}Sr_{0.8}Ti_{0.9}Mn_{0.1}O_{3+\delta}$ (LSTMO) powders were synthesized by a traditional solid-state reaction method [27]. The composition ($La_{0.2}Sr_{0.8}Ti_{0.9}Mn_{0.1}O_{3+\delta}$) was selected as the research object because this was the first study on high temperature chemical adsorption of CO_2. Fix the Mn content to be 0.1 in this study is only to preliminarily verify the possibility of remarkable adsorption of CO_2 on the manganese-doped titanate for direct carbon dioxide electrolysis. Stoichiometric amounts of La_2O_3, $SrCO_3$, MnO_2 and TiO_2 were mixed in acetone and ground in a zirconia ball mills for 5 min at the speed of 1000 round·min^{-1}. The dried powders were pressed into pellets (pressure=3.0 MPa, diameter=20 mm, thickness=3.0mm) and sintered at 1400 ºC (3.0 °C·min^{-1}) for 10 h in air. These pellets were then ground into yellowish LSTO and brown LSTMO powders, respectively. The - (SDC) powders were prepared by a combustion method using Sm_2O_3 and $Ce(NO_3)_4$•$_6H_2O$ precursors followed by a heat treatment at 800 ºC (3.0 °C·min^{-1}) for 3 h in air as described elsewhere [28-29]. The $(La_{0.8}Sr_{0.2})_{0.95}MnO_{3-\delta}$ powders were prepared in the same way while the final heat treatment was at 1100 ºC (3.0 °C·min^{-1}) for 3 h in air. Then part of the LSTO and LSTMO powders were treated in 5%H_2 at 1300 °C (3.0 °C·min^{-1}) for 10 h to introduce low oxidation states of Mn or Ti in the samples. The phase formations of the LSTO, SDC and LSM powders were tested by X-ray diffraction (XRD, 2θ=3°•min^{-1}, D/MAX2500V, Rigaku Corporation, Japan) and analyzed using GSAS software. Transmission Electron Microscopy analysis (TEM) with selected area diffraction was performed to observe the oxidized and reduced LSTO and LSTMO powders with a JEOL 2100F field emission transmission electron microscope operated at 200 kV. X-Ray Photoelectron Spectroscopy (XPS) was performed on a Thermo ESCALAB 250 using monochromatized Al Ka at hn ¼ 1486.6 eV to analyze the surface of the oxidized and reduced LSTO and LSTMO sample powders. The binding energies were calibrated to the C_{1s} peak at 284.6 eV. The TGA tests of the reduced and oxidized LSTO and LSTMO samples were conducted on a thermal analyser at 5 °C min^{-1} (DTG-60H, Shimadzu) with the flow rate of air (99.99%) at 100 ml•min^{-1}. The Pulsed Adsorption of CO_2 and Temperature Programmed Desorption (TPD) of CO_2 were recorded with a Micromeritics 2000. Here the powder samples were pre-treated at 200 °C in Ar for 1 h before Pulsed Adsorption of CO_2. The Temperature Programmed Desorption of CO_2 was tested from room temperature to 800 °C at 10 °C min^{-1} with He gas carrier. Proper amounts of LSTO and LSTMO powders were pressed into bars at the pressure of 6 MPa (40mm×5mm×3mm) and sintered in air at 1400 °C (3.0 °C·min^{-1}) for 2 h to obtain samples for conductivity tests.

About 2.0 g of LSTO and LSTMO powders were pressed into disks with diameter of 20 mm and thickness of 2 mm at the pressure of 4 MPa and then sintered at 1400 °C (3.0 °C·min^{-1}) for 10 h in air to obtain samples for ionic conductivity tests, and the relative densities reached approximately 95%, respectively. Then, some of the samples were chemically reduced at 1400 °C (3.0 °C·min^{-1}) for 10 h in 5%H_2/Ar. The ionic conductivities of the samples were tested in 5%H_2/Ar and air with electron-blocking electrode method using the DC four-terminal method an online multi-meter from about 30 to 800 °C with the temperature recorded at a step of 0.5 °C using an online system (Keithley 2000, Digital Multimeter, Keithley Instruments Inc., USA) (See SI*). The oxygen partial pressure was recorded to be approximately 1×10^{-19} atm in the reducing atmosphere of 5%H_2/Ar at 800°C with an online oxygen sensor (Type 1231, ZrO_2-based oxygen sensor, Noveltech, Australia) and an online multi-meter (Keithley 2000, Digital Multimeter, Keithley Instruments Inc., USA), respectively. As the electronic conductivity of YSZ is very small under experimental conditions, so it can be considered as a pure ionic conductor. Silver paste was printed onto both electrode surfaces for current collection in our work while Pt is sometimes utilized instead of Ag. A group of 2-mm-thick YSZ electrolyte supports were prepared by dry-pressing YSZ powders into green disks with a diameter of 20 mm and then fired at 1550 °C for 20 h in air. The two surfaces of the obtained YSZ electrolyte support were mechanically polished and then ultrasonically cleaned in distilled water. The prepared LSTO-SDC powders and LSTMO-SDC powders (at a ratio 65:35 wt %) were mixed with alpha-terpineol and appropriate amounts of cellulose additive to form a slurry and then printed onto the two surfaces of YSZ discs in area of 1.0 cm^2 to assemble symmetrical cells, respectively. The electrodes were then treated at 1000 °C (3 °C• min^{-1}) for 3 h in air [30]. The current collection

layer was constructed by printing silver paste (SS-8060, Xinluyi, Shanghai, China) on both electrode surfaces. An external circuit was applied with silver wire (0.4 mm in diameter), which was connected to current collectors using conductive adhesive (DAD87, Shanghai Research Institute for Synthetic Resins, Shanghai, China) followed by firing at 550 °C (3.0 °C·min^{-1}) for 30 min in air. The single solid oxide electrolysers were prepared with LSM-SDC anode and LSTO-SDC or LSTMO-SDC cathode and then treated in the same way at 1000 °C (3 °C·min^{-1}) for 3 h in air. The symmetrical cells with the configurations of LSTO-SDC/YSZ/LSTO-SDC and LSTMO-SDC/YSZ/LSTMO-SDC were tested in different hydrogen partial pressures and different carbon monoxide partial pressure at 800 °C using an electrochemical station (IM6, Zahner, Germany) with a frequency range of 4 M−0.1 Hz and signal strength of 10 mA, respectively. The electrode polarization resistance was calculated by modeling the spectra using Zview software. The gas flow rate was controlled using a carbon dioxide mass flow meter (D08-3F, Sevenstar, Beijing, China). The solid oxide electrolyzers with configurations of LSTO-SDC/YSZ/LSM-SDC and LSTMO-SDC/YSZ/LSM-SDC were investigated for direct carbon oxide electrolysis. The single solid oxide electrolyzers were sealed to a home-made testing jig by using ceramic paste (JD-767, Jiudian, Dongguan, China) for electrochemical measurements. The AC impedance spectroscopy (frequency range of 4 M−0.1 Hz and signal strength of 10 mV) and current-voltage curve (I-V curve, at the step of 0.004 V•s^{-1}) of the electrolysers were recorded. The electrolysis of carbon dioxide or steam was performed using an electrochemical station. The output gas from the cathode was analyzed using an online gas chromatograph (GC9790II, Fuli, Zhejiang, China) Scanning Electron Microscope (SEM, JEOL5600, Japan) was employed to observe cross-sections of the symmetrical cells and the solid oxide electrolysers.

First Principles Calculations

To understand the chemical adsorption especially at high temperatures, theoretical calculations are tentatively utilized to understand the mechanism of chemical adsorption. Our calculations were performed with density functional theory implemented in the *Vienna Ab Initio* Simulation Package (VASP) [31-32]. Within the projector augmented wave (PAW) framework, the plane-wave cutoff energy was set to 500 eV, which gives well converged relative energies for the system. The Perdew-Burke-Ernzerhof (PBE) functional [33] was used to describe exchange and correlation. In electronic and geometric optimizations, energies and residual forces were converged to 10-5 eV and 0.02 eV/Å, respectively. In order to simplify and facilitate the calculation, the creation of oxygen vacancy because of the Mn dopant and the La dopant in the A-site has been reasonably simplified to be oxygen-deficient $SrTiO_3$. The lattice parameter of $SrTiO_3$ (STO) optimized with a 13×13×13 k-point grid [34] was 3.951 Å, which is in good agreement with our experimental values. The periodic slab model was used to simulate the (001) surface of STO with an oxygen vacancy for both SrO and TiO_2 terminations. For the SrO-terminated surface, three SrO layers and two TiO_2 layers were included in the slab while for the TiO_2-terminated surface, three TiO_2 layers and two SrO layers were included. The bottom layer was fixed to its bulk geometry during optimization and other atoms were fully relaxed. A vacuum layer about 12 Å was inserted in the c direction to avoid the slab-to-slab interaction. The adsorption energy of CO_2 was calculated as $E=E_{slab}+E_{ad}-E_{tot}$ where E_{slab}, E_{ad}, and E_{tot} were the energy of the surface slab without adsorption, the energy of the CO_2 in gas phase, and the total energy of the adsorption system, respectively.

Results and discussion

Fig. 1 (a1) and (b2) show the XRD Rietveld refinement patterns of the prepared LSTO and reduced LSTO powders, respectively. The refinements of the oxidized and the reduced samples give χ^2, wR_p and R_p values of 2.068, 2.074% and 1.299% as well as 1.987, 2.410% and 1.364%, respectively, indicating a close fit to the experimental data. Based on experimental and calculated results, it is confirmed that the phase structures of both oxidized and reduced samples can be determined as perovskite structure with space group of Pm-3m [35]. The crystal cell parameter of the oxidized LSTO is determined to be 3.9108(4) Å which is slightly smaller than that of the reduced LSTO, 3.9319(0) Å. This is because titanium is generally Ti^{4+} (0.605 Å) in the oxidized LSTO while the reduced LSTO contains a part of Ti^{3+} (0.670 Å) which may give rise to expansion of the cell parameters though the oxygen loss is present after the high-temperature reductions. Nevertheless, no phase transition was observed in the LSTO even after the high-temperature treatment in a very reducing atmosphere, firmly verifying superior redox stability of the titanate ceramics. In contrast, as shown in Fig. 1 (b1) and (b2), XRD pattern of single-phase LSTMO reveals the successful partial replacement of Ti by Mn in the B site of titanate. The refinement of the oxidized and the reduced sample gives χ^2, wR_p and R_p values of 2.035, 0.826% and 0.536% as well as 1.017, 0.589% and 0.452%, respectively. The cell parameter is 3.9067(0) Å which is much smaller than that of the oxidized LSTO sample, which is because of the smaller ionic radii of the Mn^{4+} (0.530 Å). However, the cell parameter of the reduced LSTMO is increased to 3.9125(3) Å. This is because most of the Mn^{4+} and part of the Ti^{4+} have been reduced to Mn^{3+} (0.645 Å) and Ti^{3+} (0.670 Å) that have led to the expansion of the cell parameters of the reduced samples. High-resolution transmission electron microscopy (HR-TEM) analysis of the oxidized LSTMO has revealed lattice spacing of 0.390 nm (001) and 0.286 nm (110), as shown in Fig.2 (a) and (b), consistent with the separation spacing determined by the XRD analysis. The corresponding lattice spacing of the oxidized has increased from 0.277 nm (110) to the 0.289 nm (110) for the reduced LSTO firmly confirm the lattice expansion of the reduced sample as determined by the XRD analysis.

To confirm the elemental valence change, XPS analysis is performed to test the oxidized and reduced samples. All XPS spectroscopies are fitted with a Shirley-type background subtraction method. The background-functions for different spectroscopies of elements are fitted by 80% Gaussian and 20% Lorenz. As shown in Fig. S3 (a) and (b), only Ti^{4+} is observed in the oxidized LSTO sample; however, part of the Ti^{4+} is chemically reduced into Ti^{3+} by treating the LSTO samples in reducing atmosphere which significantly contributes to the electronic conductivity of the reduced LSTO sample. Similar chemical state change of Ti element has also been observed in LSTMO sample before and after reduction at high temperatures as shown in Fig. 3 (a1) and (b1). However, the XPS signal of the Ti^{4+} has been split into two sharp peaks at 457.95 eV and 458.28

eV, indicating the different chemical environments of the Ti element in the B site after the partial replacement by Mn dopant. It is supposed that the Ti4+ peak split into two different ones is due to the different chemical environments for Ti in the Mn-doped sample. The Ti and Mn may be not homogeneously distributed in the doped perovsikte and there might be presence of some short-range ordering of Ti ions in the B-site. As shown in Fig. 3 (a2) and (b2), the Mn^{3+} ($2p^{1/2}$), Mn^{4+} ($2p^{3/2}$) and Mn^{3+} ($2p^{3/2}$) peaks are observed at 653.28 eV, 640.91 eV and 642.08 eV in oxidized LSTMO sample, whereas Mn^{3+} ($2p^{1/2}$), Mn^{4+} ($2p^{3/2}$) and Mn^{3+} ($2p^{3/2}$) show peaks at 652.88 eV, 640.48 eV and 641.98 eV in reduced LSTMO sample. The XPS data reveals that Mn is in mixed chemical states of Mn^{4+}/Mn^{3+} for the Mn-doped LSTMO sample in oxidized state. The mixed chemical states of Mn^{4+}/Mn^{3+} is further confirmed by the presence of the Mn^{3+} for the oxidized LSTMO as evident in Fig. 3 (a2) though chemical states of manganese-containing compounds are mainly +4 especially in ceramic oxides. As shown in Fig. 3 (b2), the similar phenomenon of the Mn^{3+}/Mn^{4+} are observed even though the sample is strongly reduced. This can be probably ascribed to two causes: one is that adsorption of atmospheric oxygen would lead to the oxidation of Mn^{3+} to Mn^{4+} on the sample surface; the other is that there is still remaining tiny amount of Mn^{4+} in the perovsikte lattice even under very reducing atmosphere.

For the analysis of oxygen nonstoichiometry, titration techniques or thermo-gravimetry is more common. In our work, we also conducted TGA test of reduced LSTO in air to 1200 °C as shown in Fig. 4. The reduced LSTO gains the rapid weight increase of 0.56 wt% from 500 to 700 °C with complete oxidation at this temperature, which is attributed to the re-oxidation of the Ti^{3+} to Ti^{4+} in reduced LSTO. The narrow temperature range of the oxidation of the reduced LSTO further confirms the poor redox activity of Ti element. The reduced LSTO demonstrates a chemical formula of $La_{0.2}Sr_{0.8}TiO_{3.051}$ when assuming that LSTO is completely oxidized into $La_{0.2}Sr_{0.8}TiO_{3.100}$ at 700 °C, which implies that 9.8% of the Ti^{4+} has been transformed to Ti^{3+} after the reduction treatment that offers the sufficient free electron as the charge carrier for metallic electronic conduction. However, the change of the Ti^{4+} to Ti^{3+} is not accompanied by the creation of oxygen vacancy with the decrease of the coordination number of Ti but the loss of excess interstitial oxygen. In contrast, the doping of redox-active Mn significantly changes the chemical properties of the LSTMO and the transition of Mn^{4+} to Mn^{3+} would decrease the coordination number of Mn^{3+} accompanied by the creation of oxygen vacancies. As shown in Fig. 4 (b), the onset temperature of the weight gain starts from approximately 300 °C for the reduced LSTMO and the weight gradually increases by 1.2% even up to 1200 °C, confirming the excellent redox activity of the doped material. The chemical formula of the reduced LSTMO is determined to be $La_{0.2}Sr_{0.8}Ti_{0.9}Mn_{0.1}O_{3.001}$, suggesting that most of the Mn^{4+} has been reduced to Mn^{3+} accompanied by the creation of 0.05 mol oxygen vacancy per chemical formula unit. The wide temperature range of the weight gain further demonstrates the remarkable oxygen buffering capacity of the reduced LSTMO. The redox activity of Mn is higher than that of Ti in perovskite. The doping of La in the A site generates the oxygen interstitial not the reduction of Ti; however, the reduction of the sample reduces the amount of oxygen interstitials not the change of coordination number of Ti in the perovskite. In contrast, the doping of Mn makes the properties of the sample different because the reduction of the sample not only leads to the loss of oxygen interstitial but also decreases the coordination number of the doped Mn that creats the oxygen vacancies.

With the creation of oxygen vacancy in titanate, the ionic conductivity of Mn-doped titanate is expected to be improved. The ionic conductivity tests use DC polarization method with temperature ranging from 200 to 800 °C, Fig. S2 shows the schematic configuration of the cell with electronic blocking electrode. The samples pellets were plastered onto dense YSZ pellets with Ag paste, which was used to overcome the interfacial resistance. Then Ag paste was painted on the outside of both the connected samples and YSZ pellets as current collectors. In the system, the electron flux is blocked by YSZ layer because YSZ is considered to be almost a pure oxygen ion conductor. Glass seal was used to prevent oxygen leakage along the sides of the assembled samples. Applying a DC voltage on the outside of both samples and YSZ layers, a stable current can be observed at designated temperature. The transformation of oxygen and oxide ion is repeated on Ag electrode for several times in the testing system. Then the total resistance caused by double layer materials can be calculated. Therefore, the ionic conductivity of sample (σ_{ion}) can be worked out by its oxygen ionic resistance. Fig.5 (a) shows the temperature dependence of ionic conductivity of the oxidized LSTO and LSTMO in air from 400 to 800 °C, respectively. The ionic conductivities of the oxidized LSTO and LSTMO improve with temperature and finally reach 4.467×10^{-4} and 3.163×10^{-3} S•cm^{-1} at 800 °C, respectively. The introduction of redox-active Mn significantly enhances the ionic conductivity of LSTMO because of the creation of charge carrier, oxygen vacancy, in bulk. However, the pure LSTO only demonstrates conductivity 1 order of magnitude lower, which is probably attributed to the absence of sufficient oxygen vacancy as the charge carrier for the ionic conductivity. Upon reduction, LSTMO shows the improved ionic conductivity by 1 order of magnitude higher in reducing atmosphere at intermediate temperatures. At this stage, the oxygen vacancies are 0.05 mol per chemical formula unit for the reduced LSTMO, which is expected to substantially increase the ionic conductivity of the reduced LSTMO. The conductivity finally reaches as high as 1.413×10^{-2} S•cm^{-1} at 800°C in reducing atmosphere, which is 1 order of magnitude higher than 1.122×10^{-3} S•cm^{-1} for the reduced LSTO. It is expected that the oxygen vacancy defect site is able to accommodate the carbon dioxide molecules to act the chemical adsorption behavior. To investigate the adsorption of CO_2 on the reduced LSTO and LSTMO, Pulsed Adsorption of CO_2 and Temperature Programmed Desorption are performed to study the physical and chemical adsorptions of CO_2 on powder samples. Fig.6 (a) and (b) show the CO_2 adsorption and desorption on the LSTO sample, where the total adsorption of CO_2 is around 0.0054 ml•m$^{-2}_{cata}$ which is mainly dominated by physical adsorption and weak chemical adsorption. It is observed that the physical desorption of the CO_2 is completed below 100 °C. The chemical desorption as shown in Fig.6 (b) at approximately 200, 300 and 400 °C are related to the basic sites and basic property of the surface of the reduced $La_{0.2}Sr_{0.8}TiO_{3.055}$ as expected [24]. On the other hand, the dipole–dipole coupling between CO_2 molecules and particle surface may promote chemical adsorption that results in chemical desorption in a similar temperature region at 200 °C. In contrast, the total adsorption of CO_2 is significantly enhanced

to 0.0454 ml•m^{-2}_{cata} which is approximately 1 order of magnitude higher than that of pure LSTO sample. Similar chemical desorption of CO_2 has also been observed in the temperature range of 200-400 °C for the reduced LSTMO sample. However, the strongest chemical desorption is remarkably extended to as high as approximately 800 °C as observed in Fig.5 (d). This indicates the presence of sufficient oxygen vacancy defects not only substantially improves the chemical adsorption but also significantly extends the chemical desorption to high temperature region.

To understand the chemical adsorption especially at high temperatures, theoretical calculations are tentatively utilized to understand the mechanism of chemical adsorption. In order to simplify and facilitate the calculation, the creation of oxygen vacancy because of the Mn dopant and the La dopant in the A-site has been reasonably simplified to be oxygen-deficient $SrTiO_3$. Our first-principles calculations also give stable adsorption configurations of CO_2 on STO with an oxygen vacancy for both SrO-terminated and TiO_2-terminated surfaces. The adsorption structure on SrO-terminated surface is shown in Fig. 7 (a1) and (a2). The distances between the two oxygen atoms in CO_2 to their nearest strontium atoms are both 2.417 Å, smaller than the SrO bond length in bulk STO whose experimental value is 2.767 Å [36], indicating a strong chemical adsorption of CO_2 on the defected surfaces. The corresponding adsorption energy is calculated to be 2.14 eV. Similarly, the distances of the oxygen atoms in CO_2 to their nearest titanium atoms are 2.006 and 2.009 Å for the TiO_2-terminated surface as shown in Fig. 7 (b1) and (b2), respectively, quite close to the experimental value 1.952 Å [37] in bulk STO. Comparing to pristine STO surfaces [38], the CO_2 adsorbed on a defected site with oxygen vacancy is more stable. The strong bonding between the CO_2 molecules and the defected sites substantially extend the desorption temperature to as high as approximately 800 °C which is quite close to, 800-830 °C, the decomposition temperature of $SrCO_3$ [39]. In addition to the strong bonding, the linear CO_2 molecules have accordingly been robustly bended with large angles. This distorted CO_2 molecules are expected to be strongly activated on the defected surface with sufficient oxygen vacancies.

Fig. 8 presents the microstructures of the YSZ electrolyte-supported half cells based on LSTMO and LSTO electrodes, respectively. It can be found that the LSTMO and LSTO electrodes are porous, and they adhere well to the dense YSZ electrolyte. Fig. 9 shows the AC impedance of the symmetric cells based on the LSTO and LSTFO tested at 800 °C in different hydrogen partial pressure (10, 20, 40, 60, 80 and 100%H_2), respectively. The series resistance (R_s) and the polarization resistance (R_p), depicted by the first intercept and the difference between the first and second intercepts, were calculated by Zview software as reported in our previous work [40]. The ionic resistance of the YSZ electrolyte which mainly contributes to the R_s is generally stable in a wide range of hydrogen partial pressure. However, as shown in Fig. 9 (a1) and (a2), the Rp of the symmetric cell based on LSTO-SDC decreases from approximately 28 to 9 Ω•cm^2 with the hydrogen partial pressure ranging from 10% to 100%, suggesting that the stronger reducing atmosphere is beneficial to the improvement of the electrode polarizations. In contrast, the R_p of the symmetric cell based on LSTMO-SDC significantly decreases with increasing hydrogen concentration from about 4 to 2 Ω•cm^2, which is probably due to the enhanced charge transfer and species diffusion in this composite electrode [40]. Similar behavior has also been observed for both LSTO and LSTMO electrode in symmetric cells in CO/Ar atmosphere with CO concentration ranging from 1% to 5%. In this case, a stronger reducing atmosphere with higher content of CO is also favourable to increasing electrical conductivity of the reduced LSTO and LSTMO for improved electrode performances. On the other hand, this redox-stable electrode shows the promising polarizations even in a less reducing atmosphere, which necessary for a direct electrolysis of carbon dioxide or steam at higher temperatures.

The direct electrolysis of pure carbon dioxide (100%CO_2) is investigated in two kinds of solid oxide electrolyzers with configurations of (cathode) LSTO-SDC/YSZ/LSM-SDC (anode) and (cathode) LSTMO-SDC/YSZ/LSM-SDC (anode) under a series of applied voltages ranging from 0 to 2.0 V at 800 °C, respectively. Fig. 11 shows the typical curves of the voltage versus current density (I-V curves) of the electrolyzers for the direct carbon dioxide electrolysis. The change in the slope of the I-V curves at approximately 1.0 V where the onset voltage of the electrolysis is anticipated indicates that there exist two different cell processes in the two voltage regions: (a) the electrochemical reduction of the cathodes and oxidation of the anodes at low voltages; (b) the carbon dioxide electrolysis at high voltages.The maximum current density reaches 120 mA•cm^{-2} at 2.0 V based on the LSTO-SDC cathode at 800 °C. In contrast, the cell based on LSTMO cathode is greatly improved and the current densities finally reach approximately 250 mA•cm^{-2} under the same conditions. Above 1.1 V, the current densities of the LSTMO electrodes increase steeply compared to the bare LSTO electrode, which indicates that the LSTMO-SDC electrode significantly enhances the cell performance for steam electrolysis. The chemical adsorption of CO_2 in the LSTMO cathode substantially contributes to the improved cell performances. The enhanced ionic conductivity of the LSTMO is also expected to improve the charge transfer in the composite electrode. In order to study the resistance change of the electrolyzer, the dV/dI curve (total cell resistance) was plotted versus applied voltage and current density as shown in Fig. S5.

Fig. 12 shows the in-situ AC impedance spectroscopy under a series of applied voltages ranging from 1.2 to 2.0 V at 800 °C in based on LSTO and LSTMO cathodes, respectively. It is observed that R_s values are stabilized at approximately 2.5Ω•cm^2, whereas R_p values considerably improve as applied voltage increase from 1.2 to 2.0 V. It is assumed that increasing the voltage activates the electrodes to the extent that R_p decreases remarkably. Increasing the voltage is expected to improve electrode polarization, following the improved kinetic process of the electrode. The applied voltage gradually electrochemically reduces the composite cathode to improve the mixed conductivity and then therefore accordingly enhances the electrocatalytic activity of the composite electrode. Two semicircles are noted on the impedance spectra: the high-frequency arcs (R_1) and low-frequency arcs (R_2). At high frequency, R_1 of the solid oxide electrolysers with cathodes based on bare LSTO is stabilized approximately 2.0 Ω•cm^2or improving in a narrow range in a wide voltage range. In contrast, the R_1 for the cell with LSTMO cathode is significantly decreased to approximately 0.5 Ω•cm^2

and is further enhanced under high applied potentials. The R_1 is an indication of charge transfer at high frequency and the LSTMO cathode with improved R_1 firmly shows that the increased oxide-ion conductivity of LSTMO significantly benefits the charge transfer and accordingly reduces the high-frequency polarization resistance. At low frequency, it is observed that the mass transfer, R_2, dominates the electrode process of the solid oxide electrolysers, which is due to the dissociative adsorption, gas conversion and species transfer in the composite electrodes. The R_2 remarkably improves from 5 to 2 $\Omega\bullet cm^2$ for the cell based on LSTO cathode with the applied voltage ranges from 1.2 to 2.0 V, suggesting the improved kinetics of gas conversion at high voltages. In contrast, the R_2 is significantly reduced to 3 $\Omega\bullet cm^2$ at low voltages and further enhanced to 1 $\Omega\bullet cm^2$ at high voltages for the cell based on LSTMO cathode, demonstrating the significantly improved mass transfer because of the remarkable chemical adsorption of CO_2 in the composite cathode. Fig. S6 shows the R_p versus i.R corrected voltages during the CO_2 electrolysis at 800 ºC. These data allow further understanding of the changes under different voltages where the voltages of i.R were subtracted. To study the electrolysis performance of the solid oxide electrolyzers with LSTMO and LSTO cathodes, both cells are operated with the cathodes fed pure CO_2 at 800 °C as shown in Fig. 13. The current density with LSTMO-SDC cathode still reaches 70, 150 and 240 $mA\bullet cm^{-2}$ at 1.2, 1.6 and 2.0 V, respectively, which are 2-3 times higher in contrast to the cell performance with LSTO cathode under the same conditions. The production rates of CO reach as high as 0.1-0.2 $ml\bullet cm^{-2}\bullet min^{-1}$ for the cell with LSTO cathode at 1.2-2.0 V; however, the generation rates are remarkably enhanced to as high as 0.3, 0.6 and 1.1 $ml\bullet cm^{-2}\bullet min^{-1}$ at 1.2, 1.6 and 2.0 V, respectively. As shown in Fig. 13 (c), the current efficiencies are only 55-65% for the cell with LSTO cathode at 1.2-2.0 V; however, the efficiencies reach 85-90% at low voltages and further improve to approximately 100% for the cell with LSTMO cathode at high voltages. In order to further study the electrolysis performance of the solid oxide electrolyzers with LSTMO and LSTO cathodes, both cells were operated with the cathodes fed $3\%H_2O/5\%H_2$/Ar and $3\%H_2O$/Ar at 800 °C, respectively. As shown in Part 2 of the supporting information, significant improvements in electrochemical performance and current efficiency were achieved with the LSTMO electrode for steam electrolysis with or without a flowing reducing gas over the cathodes. The current efficiency with LSTMO cathode was enhanced approximately by 12% and 28% compared to the values with LSTO cathode under 2.0 V of applied voltage at 800 °C with a flow of $3\%H_2O/5\%$ H_2/Ar and 3% H_2O/Ar to cathodes, respectively.

Conclusions

In this work, the remarkable chemical adsorption of CO_2 at high temperature has been achieved by introducing the oxygen vacancy defect sites in perovsikte manganese-doped titanate. The defected sites with oxygen vacancies offer the proper space to accommodate the CO_2 molecules accompanied by the formation of strong bonding between the CO_2 molecules and the defected substrates. This specific phenomenon significantly enhances the chemical adsorption of CO_2 and further extends the strong chemical desorption to high temperature region, which is extremely important for high temperature electrolysis of CO_2 in solid oxide electrolysers. The ionic conductivities of the Mn-doped titanate are accordingly enhanced by 1-2 orders of magnitude at intermediate temperatures in reducing or oxidizing atmospheres. In addition to the promising electrode polarization based on Mn-doped cathode, the highest current efficiencies of approximately 100% are obtained for the direct electrolysis of CO_2 in an oxide-ion-conducting solid oxide electrolyser.

Affiliations

[a]*Key Laboratory of Advanced Functional Materials and Devices of Anhui Province & School of Materials Science and Engineering, Hefei University of Technology, No.193 Tunxi Road, Hefei, Anhui 230009, China. Email: xiekui@hfut.edu.cn; ycwu@hfut.edu.cn.*

[b]*Hefei National Laboratory for Physical Sciences at the Microscale, University of Science and Technology of China, No.96 Jinzhai Road, Hefei, Anhui 230026, China*

Contributions

The # indicates the equal contributions of WQ, YG and DY. WQ and YG conducted the experiment. DY and ZL performed the theory calculations. KX and YW supervised the experiments. WQ and KX drafted the manuscript. All authors were involved in the data analysis and discussions.

Acknowledgements

This work is financially supported by the Natural Science Foundation of China (NSFC) No. 21303037, China Postdoctoral Science Foundation No. 2013M53150, the Ministry of Education of Overseas Returnees Fund No.20131792 and the Fundamental Research Funds for the Central Universities No. 2012HGZY0001.

† Electronic Supplementary Information (ESI) available: [details of any supplementary information available should be included here]. See DOI: 10.1039/b000000x/

References

1 R. Lan, S.W. Tao, J.T.S. Irvine, *Energy Environ. Sci.*, 2013, 3,438-441.
2 X.M. Ge, S.H. Chan, Q.L. Liu, Q. Sun. *Adv. Energy Mater.*, 2012, 2, 1156-1181.
3 G. Tsekouras, J. T. S. Irvine, *J. Mater. Chem.,* 2011, 21, 9367-9376.
4 A. Lashtabeg, S. J. Skinner, *J. Mater. Chem.,* 2006,16,3161-3170.
5 M. A. Laguna-Bercero, J. A. Kilner and S. J. Skinner, *Chem. Mater.,* 2010, 22, 1134-1141.
6 C.L. Yang, W. Li, S.Q. Zhang, L. Bi, R.R. Peng, C.S. Chen, W. Liu, *J. Power Sources,* 2009, 187, 90-92.
7 K.V. Hansen, K. Norman, M. Mogensen. *J. Electrochem. Soc.*, 2004, 151, 1436-1444.
8 K.V. Jensen, S. Primdahl, I. Chorkendorff, M. Mogensen. *Solid State Ionics*, 2001, 144, 197-209.
9 X.D. Yang, J.T.S. Irvine. *J. Mater. Chem.*, 2008, 18, 2349-2354.
10 S. W. Tao, J. T. S. Irvine, *Nat. Mater.*, 2003, 2, 320-323.
11 S.S. Xu, S.S. Li, Y, Gan, Y.X. Li, K. Xie, *J. Power Sources*, 2013, 230, 115- 121.
12 G.J. Wu, K. Xie, Y.C. Wu, W.T. Yao, *J. Power Sources*, 2013, 232, 187-192.
13 G. Tsekouras, D. Neagu, J.T.S. Irvine, *Energy Environ. Sci.*, 2013,6, 256-266.

14 D. Neagu, J. T. S. Irvine , *Chem. Mater.*, 2010, 22, 5042-5053.
15 Y.X. Li, Y. Gan, S.S. Li, Y. Wang, H.F. Xiang, K. Xie, *Phys Chem Chem Phys*, 2012,14:15547-15553.
16 A. Hauch, S.D. Ebbesen, S.H. Jensen, M. Mogensen. *J. Mater. Chem.*, 2008, 18, 2331-2340
17 X.L. Yue, J.T.S. Irvine, *J. Electrochem. Soc.*, 2012, 159, F442-F448.
18 X.L. Yue, J.T.S. Irvine, *Solid State Ionics*, 2012, 225, 131-135.
19 C. Graves, S.D. Ebbesen, M. Mogensen, *Solid State Ionics*, 2011, 192 (1), 398-403.
20 Z.L. Zhan, W. Kobsiriphat, J.R. Wilson, M. Pillai, I. Kim, S.A. Barnett, *Energy Fuels*, 2009, 23, 3089-3096.
21 R.A. Khatri, S.S.C. Chuang, Y. Soong, M. Gray, *Energy Fuels*, 2006, 20, 1514-1520.
22 J.C. Hicks, J.H. Drese, D.J. Fauth, M.L. Gray, G.G. Qi, C.W. Jones, *J. Am. Chem. Soc.*, 2008, 130, 2902- 2903.
23 W. F. Schneider, J. Phys. Chem. B, 2004, 108, 273-282.
24 L.F. Liao, C.F. Lien. D.L. Shieh, M.T. Chen, J.L. Lin, *J. Phys. Chem. B*, 2002, 106, 11240-11245.
25 T.L. Thompson, O. Diwald, J.T.Y. Jr, *J. Phys. Chem. B*, 2003, 107, 11700-11704.
26 M. Nolan, J. Phys. Chem. C, 2009, 113, 2425-2432.
27 S.S. Li, Q.Q. Qin, K. Xie, Y. Wang, Y.C. Wu, *J. Mater. Chem. A*, 2013, 1, 8984-8993.
28 L. Zhao, J. Shen, B. He, F. Chen, C.R. Xia, *Int. J. Hydrogen Energy*, 2011, 36, 3658-3665.
29 L. Wu, S. Wang, S. Wang, C.R. Xia, *J. Power Sources*, 2013, 240, 241-244
30 Y.X. Li, Y. Wang, W. Doherty, K. Xie, Y.C. Wu, *ACS Appl. Mater. Interfaces*, 2013, 5, 8553-8562.
31 G. Kresse and J. Furthmüller, *Comput. Mater. Sci.*, 1996, 6, 15.
32 G. Kresse and J. Furthmüller, *Phys. Rev. B,* 1996, 54, 11169.
33 J. P. Perdew, K. Burke and M. Ernzerhof, *Phys. Rev. Lett.*, 1996, 77, 3865.
34 M. Methfessel and A. Paxton, *Phys. Rev. B*, 1989, 40, 3616.
35 A.D. Aljaberi, J.T.S. Irvine, *J. Mater. Chem. A*, 2013, 1, 5868-5874.
36 Y. Kuroiwa, S. Aoyagi and A. Sawada, *J. Korean Phys. Soc.*, 2003, 42, 1425.
37 L. F. Silva, W. Avansi, J. Andrés, C. Ribeiro, M. L. Moreira, E. Longo and V. R. Mastelaro, *Phys. Chem. Chem. Phys.*, 2013, 15, 12386.
38 J. D. Baniecki, M. Ishii, K. Kurihara and K. Yamanaka, *Phys. Rev. B*, 2008, 78, 195415.
39 I. Arvanitidis, DuSichen, S. Seetharaman, H.Y. Sohn, *Metall. Mater. Trans. B*., 1997, 28, 1603-1608.
40 Y.X. Li, L.M. Yang, Y. Wang, W. Doherty, K. Xie, Y.C. Wu, *J. Power Sources*, 2013, DOI: 10.1016/j.jpowsour.2013.12.046.

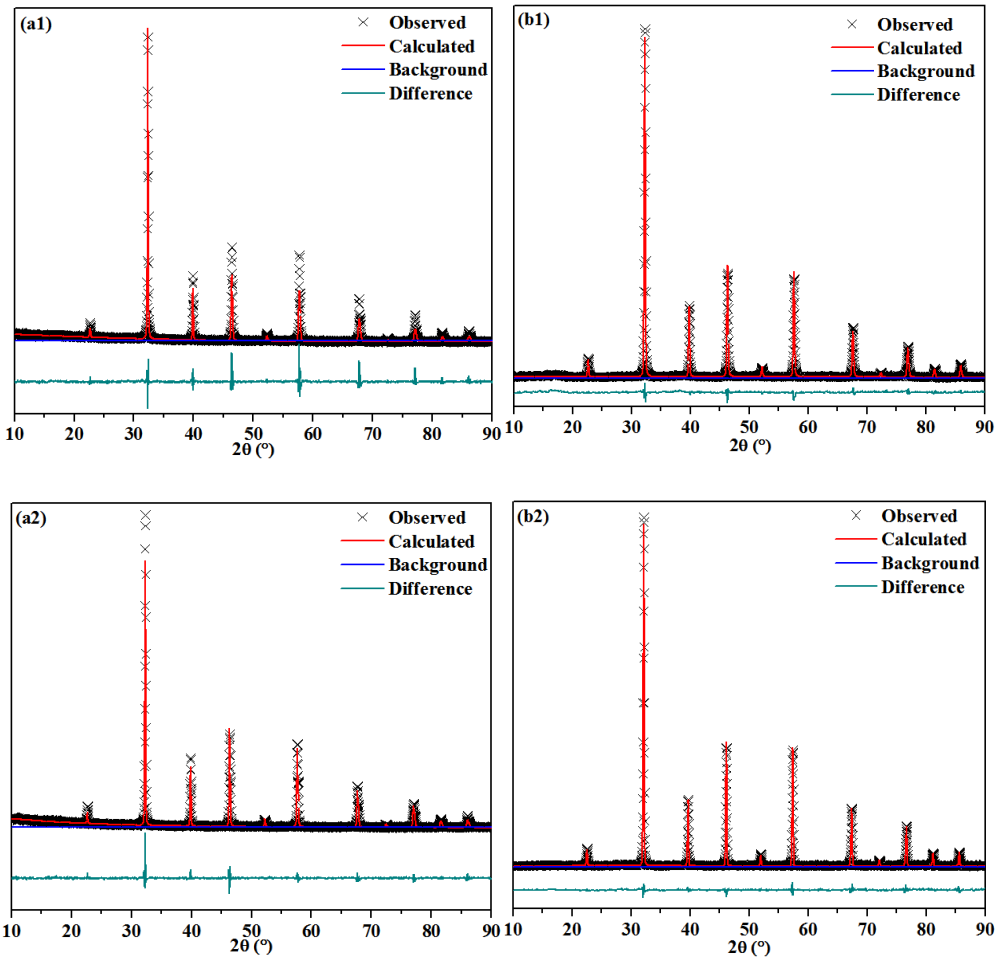

Fig.1 XRD Retvield refinement of the oxidized $La_{0.2}Sr_{0.8}TiO_{3+\delta}$ (LSTO, a1), reduced $La_{0.2}Sr_{0.8}TiO_{3+\delta}$ (LSTO, a2), oxidized $La_{0.2}Sr_{0.8}Ti_{0.9}Mn_{0.1}O_{3+\delta}$ (LSTMO, b1) and reduced $La_{0.2}Sr_{0.8}Ti_{0.9}Mn_{0.1}O_{3+\delta}$ (LSTMO, b2) powders.

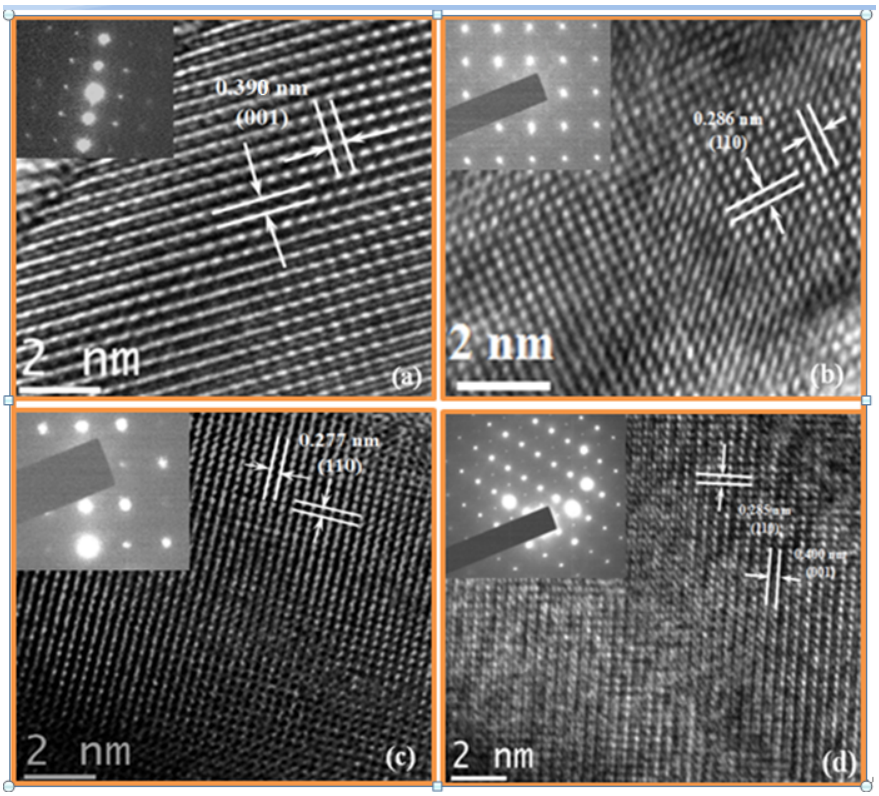

Fig.2 The TEM graph of the oxidized $La_{0.2}Sr_{0.8}Ti_{0.9}Mn_{0.1}O_{3+\delta}$ (LSTMO, a), reduced $La_{0.2}Sr_{0.8}Ti_{0.9}Mn_{0.1}O_{3+\delta}$ (LSTMO, b), oxidized $La_{0.2}Sr_{0.8}TiO_{3+\delta}$ (LSTO, c) and reduced $La_{0.2}Sr_{0.8}TiO_{3+\delta}$ (LSTO, d).

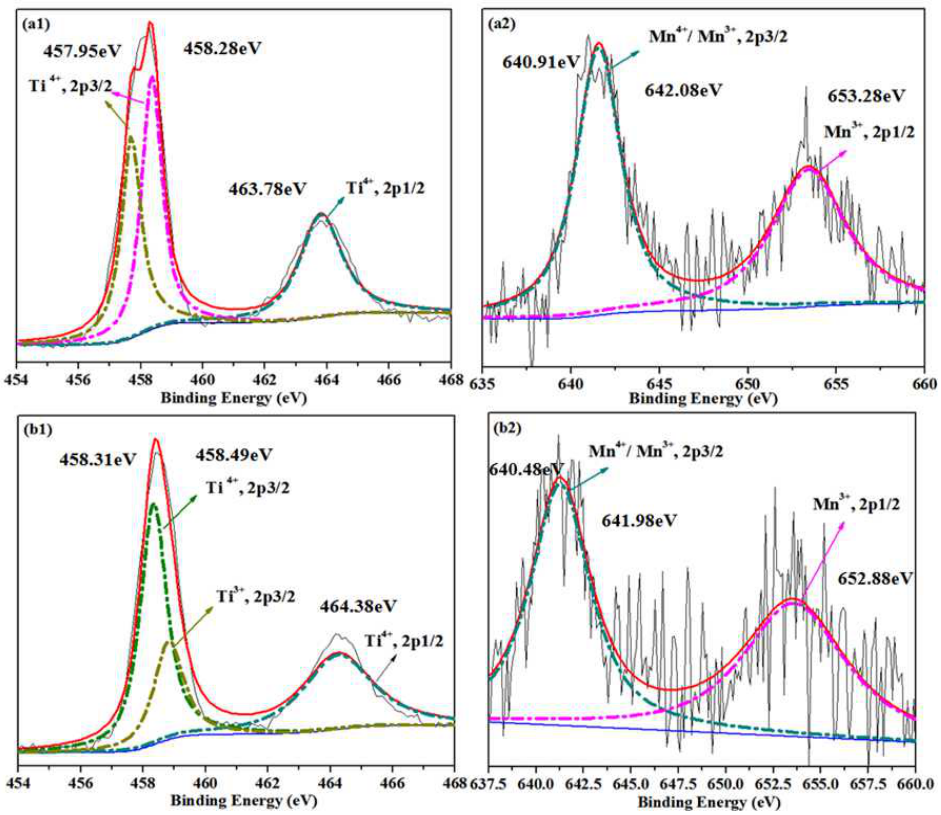

Fig.3 XPS results for Ti (a1) and Mn (a2)in the oxidized $La_{0.2}Sr_{0.8}Ti_{0.9}Mn_{0.1}O_{3+\delta}$ (LSTMO) ; Ti (b1) and Mn (b2) in the reduced $La_{0.2}Sr_{0.8}Ti_{0.9}Mn_{0.1}O_{3+\delta}$ (LSTMO).

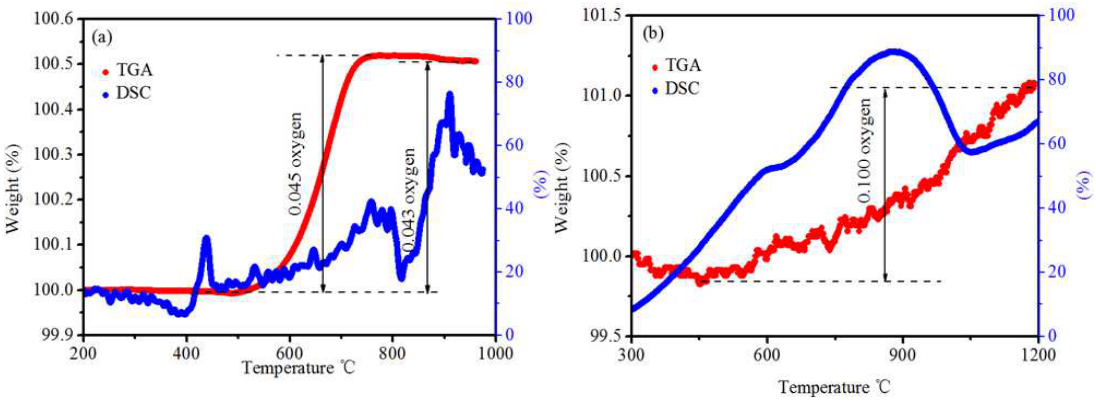

Fig.4 The TGA and DSC results of the reduced $La_{0.2}Sr_{0.8}TiO_{3+\delta}$ (LSTO, a) and the reduced $La_{0.2}Sr_{0.8}Ti_{0.9}Mn_{0.1}O_{3+\delta}$ (LSTMO, b) from room temperature to 1200°C in air.

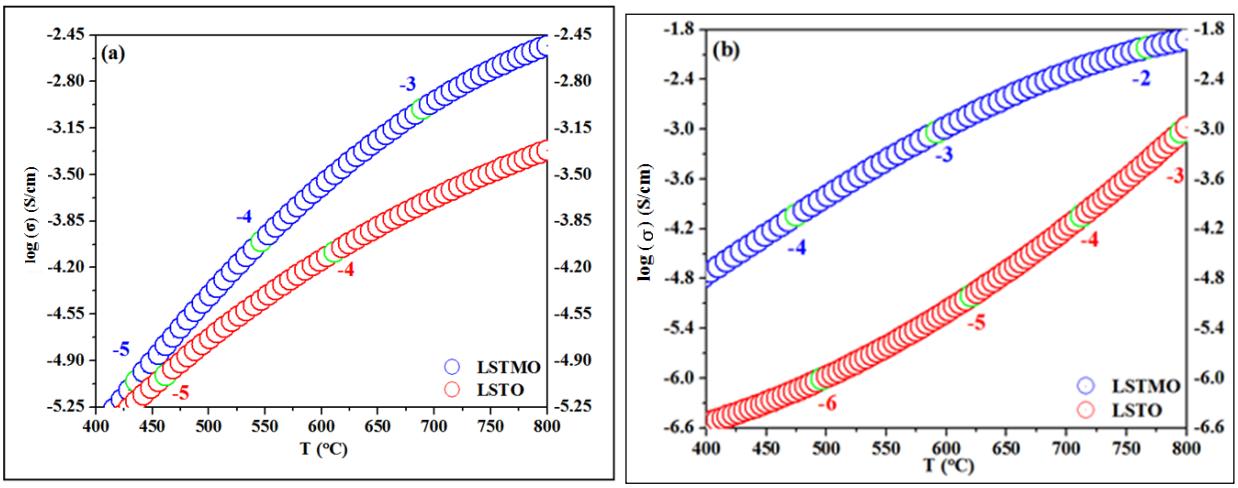

Fig.5 The dependence of ionic conductivities on temperature of the oxidized $La_{0.2}Sr_{0.8}TiO_{3+\delta}$ (LSTO) and $La_{0.2}Sr_{0.8}Ti_{0.9}Mn_{0.1}$(LSTMO) in air (a) and the reduced $La_{0.2}Sr_{0.8}TiO_{3+\delta}$ (LSTO) and $La_{0.2}Sr_{0.8}Ti_{0.9}Mn_{0.1}$(LSTMO) in 5%$H_2$/Ar (b).

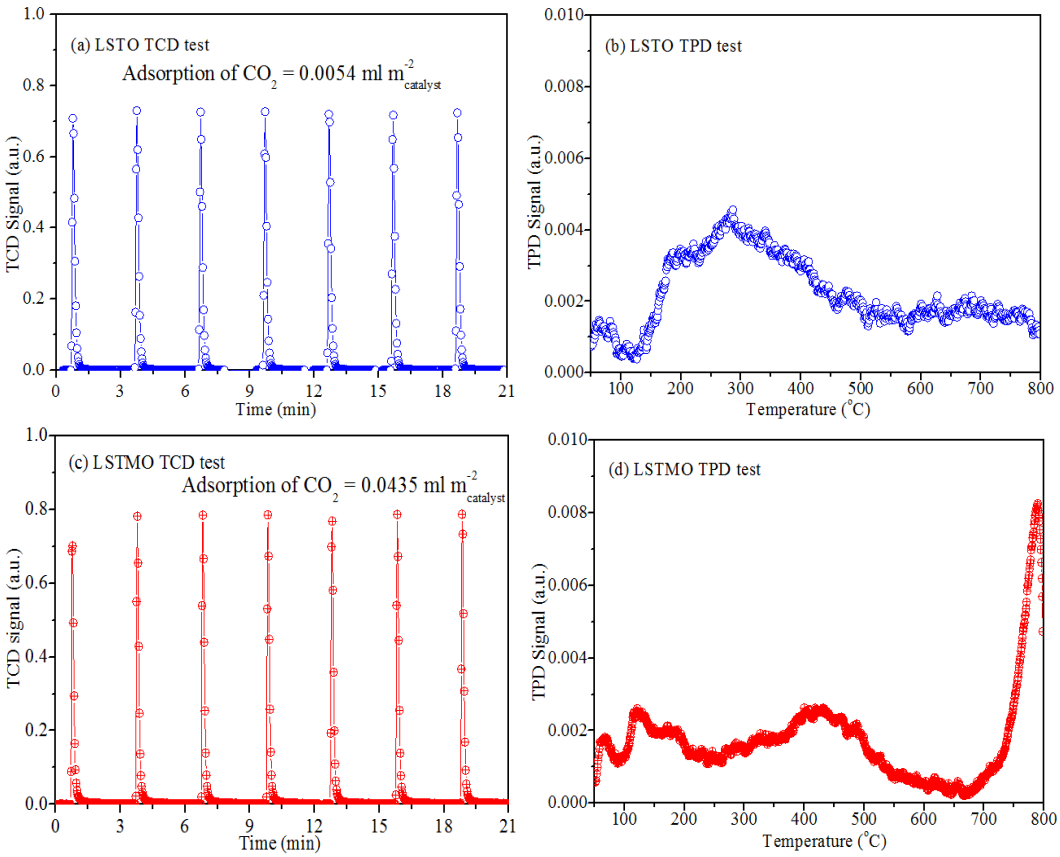

Fig.6 Adsorption and desorption of CO_2 on the surface of reduced $La_{0.2}Sr_{0.8}TiO_{3+\delta}$ (LSTO) and $La_{0.2}Sr_{0.8}Ti_{0.9}Mn_{0.1}$(LSTMO) powders.

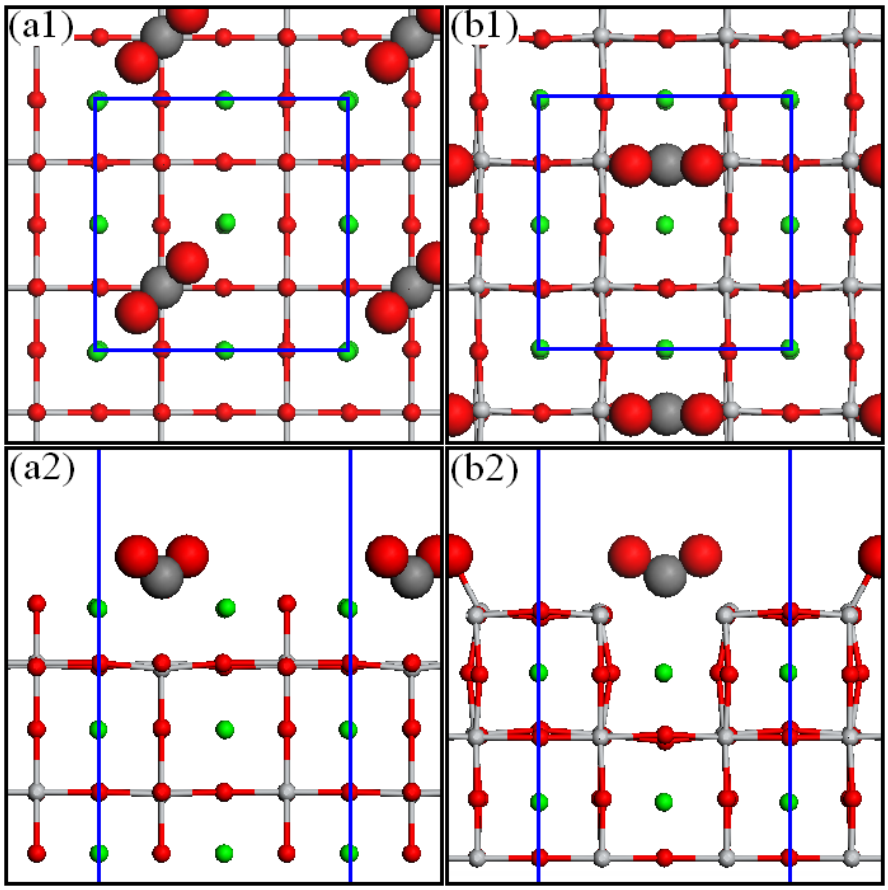

Fig. 7 Different adsorption configurations of CO_2 on (a) SrO-terminated surface and (b) TiO_2-terminated surface of STO with an oxygen vacancy. The upper panels show top views while lower panels give side views. Unit cells used in calculations are marked in blue rectangles. Strontium is in green, titanium in pale, oxygen in red, and carbon in gray.

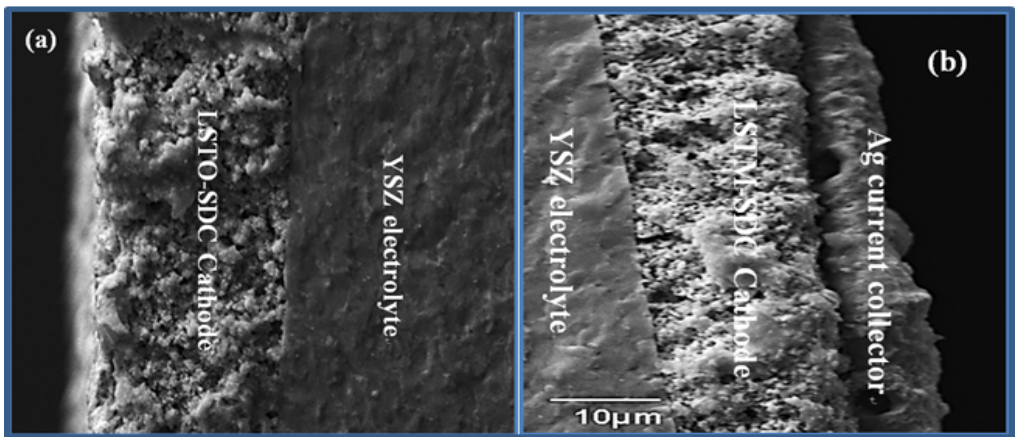

Fig.8 SEM picture of the (a) $La_{0.2}Sr_{0.8}TiO_{3+\delta}$-$Ce_{0.8}Sm_{0.2}O_{2-\delta}$ (LSTO-SDC) and (b) $La_{0.2}Sr_{0.8}Ti_{0.9}Mn_{0.1}$-$Ce_{0.8}Sm_{0.2}O_{2-\delta}$ (LSTMO-SDC) electrodes on YSZ electrolyte.

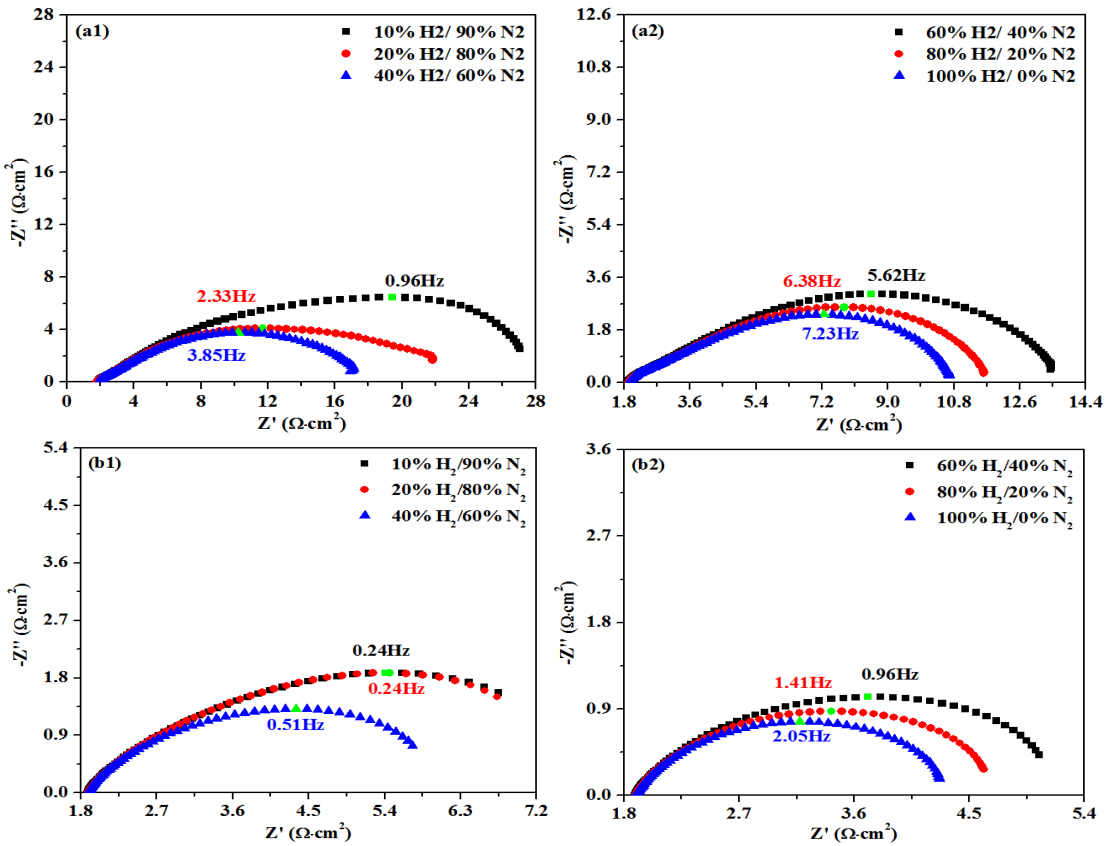

Fig.9 In-situ AC impedance of symmetric SOEs with cathodes based on (a1) (a2) $La_{0.2}Sr_{0.8}TiO_{3+\delta}$-$Ce_{0.8}Sm_{0.2}O_{2-\delta}$ (LSTO-SDC) and (b1) (b2) $La_{0.2}Sr_{0.8}Ti_{0.9}Mn_{0.1}$-$Ce_{0.8}Sm_{0.2}O_{2-\delta}$ (LSTMO-SDC) electrodes under different hydrogen partial at 800 ºC.

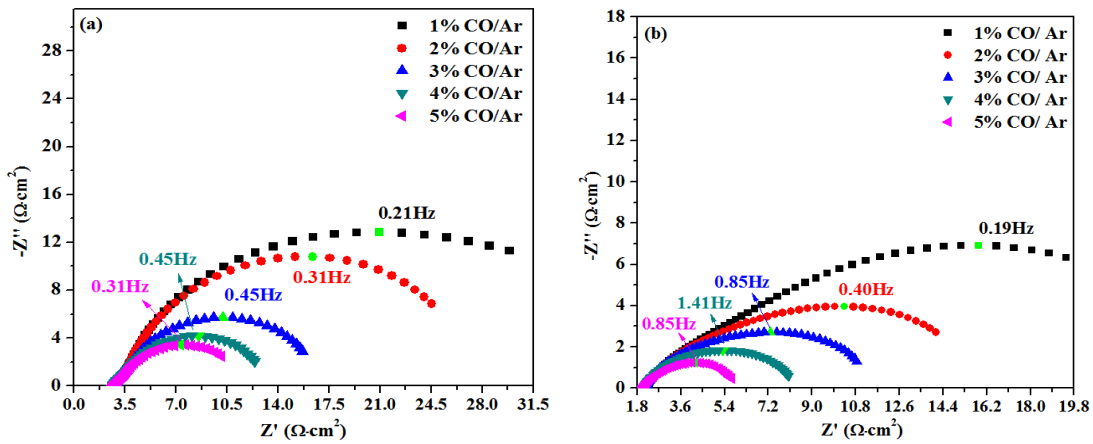

Fig.10In-situAC impedance of symmetric cells with cathodes based on (a) $La_{0.2}Sr_{0.8}TiO_{3+\delta}$-$Ce_{0.8}Sm_{0.2}O_{2-\delta}$ (LSTO-SDC) and (b) $La_{0.2}Sr_{0.8}Ti_{0.9}Mn_{0.1}$-$Ce_{0.8}Sm_{0.2}O_{2-\delta}$ (LSTMO-SDC) tested in CO/Ar with different CO concentrations.

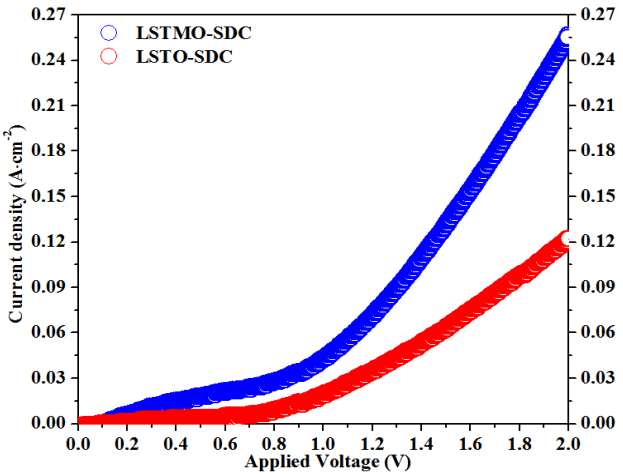

Fig.11 I-V curves of SOEs with cathodes based on $La_{0.2}Sr_{0.8}TiO_{3+\delta}$-$Ce_{0.8}Sm_{0.2}O_{2-\delta}$ (LSTO-SDC) and $La_{0.2}Sr_{0.8}Ti_{0.9}Mn_{0.1}$-$Ce_{0.8}Sm_{0.2}O_{2-\delta}$ (LSTMO-SDC) for CO2 electrolysis.

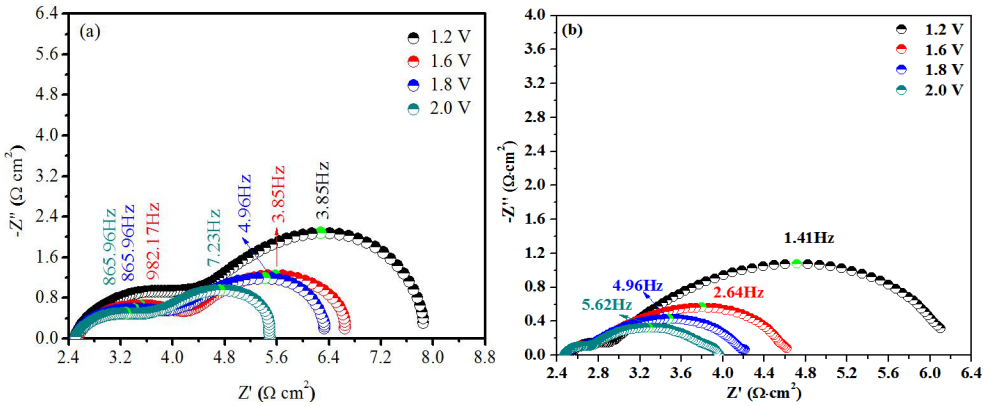

Fig.12 AC impedance of single electrolysers with cathodes based on (a) $La_{0.2}Sr_{0.8}TiO_{3+\delta}$-$Ce_{0.8}Sm_{0.2}O_{2-\delta}$ (LSTO-SDC) and (b) $La_{0.2}Sr_{0.8}Ti_{0.9}Mn_{0.1}$-$Ce_{0.8}Sm_{0.2}O_{2-\delta}$ (LSTMO-SDC) under different applied potentials at 800 ºC in CO_2.

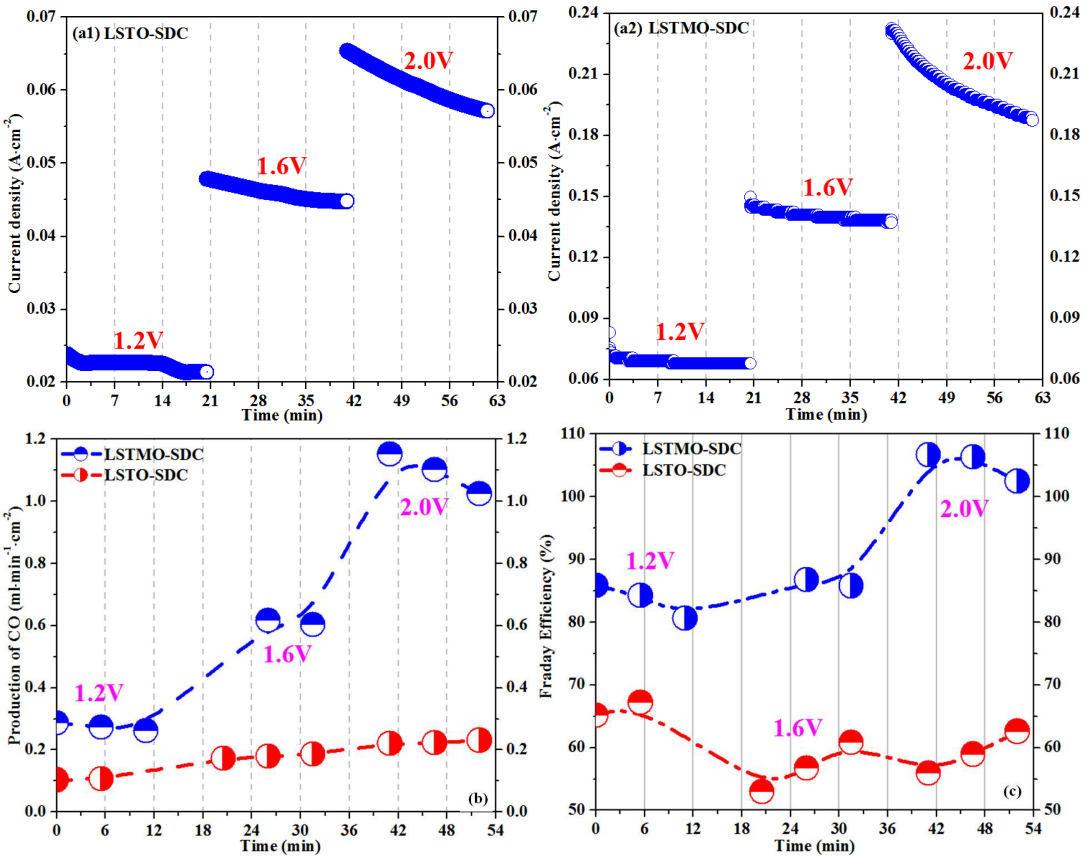

Fig.13 (a1) (a2) Short-term performance of electrolyzing CO_2; (b) The production of CO during the electrolysis and (c) its corresponding Faraday efficiency.

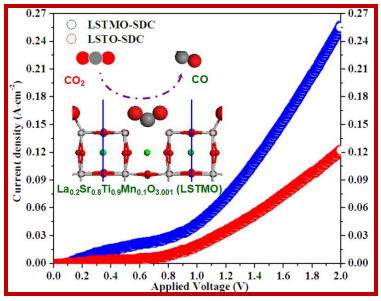

Remarkable chemical adsorption of CO_2 has been achieved in titanate with significant concentration of oxygen vacancies towards the efficient direct CO_2 electrolysis in solid oxide electrolysers.